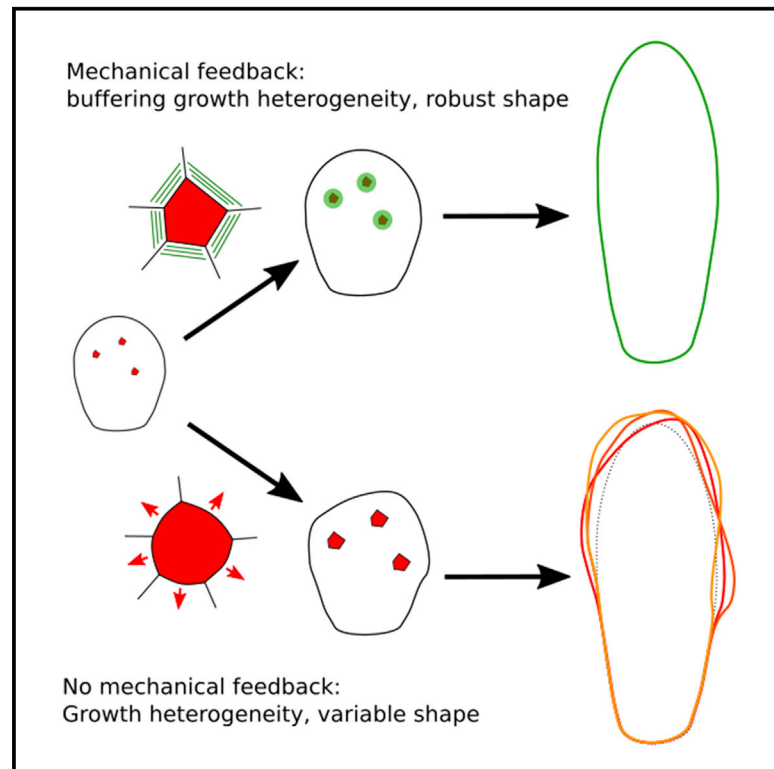**Article**

Mechanical Shielding of Rapidly Growing Cells Buffers Growth Heterogeneity and Contributes to Organ Shape Reproducibility

Graphical Abstract

Authors

Nathan Hervieux, Satoru Tsugawa, Antoine Fruleux, ..., Richard S. Smith, Chun-Biu Li, Olivier Hamant

Correspondence

olivier.hamant@ens-lyon.fr

In Brief

Hervieux et al. show that local growth heterogeneities within an epithelium trigger mechanical conflicts and consequently a stereotypical cytoskeletal response in adjacent cells. This leads to the mechanical shielding of rapidly growing cells, thus buffering growth heterogeneities and finally contributing to organ shape reproducibility.

Highlights

- Growth heterogeneity generates stereotypical pattern of tensile stress

- Local mechanical conflicts impact microtubule behavior in adjacent cells

- Trichomes are mechanically isolated by the microtubule response to stress

- Organ shape reproducibility can be achieved by filtering out fast-growing cells

CellPress

Mechanical Shielding of Rapidly Growing Cells Buffers Growth Heterogeneity and Contributes to Organ Shape Reproducibility

Nathan Hervieux,[1,6,7] Satoru Tsugawa,[2,5,6,8] Antoine Fruleux,[1] Mathilde Dumond,[1] Anne-Lise Routier-Kierzkowska,[3,9] Tamiki Komatsuzaki,[2] Arezki Boudaoud,[1] John C. Larkin,[4] Richard S. Smith,[3] Chun-Biu Li,[2,5] and Olivier Hamant[1,10,*]

[1]Laboratoire de Reproduction et Développement des Plantes, Université de Lyon, UCB Lyon 1, ENS de Lyon, INRA, CNRS, 46 Allée d'Italie, 69364 Lyon Cedex 07, France
[2]Research Institute for Electronic Science, Hokkaido University, Kita 20 Nishi 10, Kita-ku, Sapporo 001-0020, Japan
[3]Department of Comparative Development and Genetics, Max Planck Institute for Plant, Breeding Research, Carl-von-Linné-Weg 10, 50829 Köln, Germany
[4]Department of Biological Sciences, Louisiana State University, Baton Rouge, LA 70803-1715, USA
[5]Department of Mathematics, Stockholm University, 106 91 Stockholm, Sweden
[6]These authors contributed equally
[7]Present address: The Department of Physiology, Development and Neuroscience, University of Cambridge, Downing Street, Cambridge CB2 3DY, UK
[8]Present address: Theoretical Biology Laboratory, RIKEN, Wako 351-0198, Japan
[9]Present address: Institut de Recherche en Biologie Végétale, Département de Sciences Biologiques, Université de Montréal, 4101 rue Sherbrooke est, Montréal, QC H1X 2B2, Canada
[10]Lead Contact
*Correspondence: olivier.hamant@ens-lyon.fr
https://doi.org/10.1016/j.cub.2017.10.033

SUMMARY

A landmark of developmental biology is the production of reproducible shapes, through stereotyped morphogenetic events. At the cell level, growth is often highly heterogeneous, allowing shape diversity to arise. Yet, how can reproducible shapes emerge from such growth heterogeneity? Is growth heterogeneity filtered out? Here, we focus on rapidly growing trichome cells in the *Arabidopsis* sepal, a reproducible floral organ. We show via computational modeling that rapidly growing cells may distort organ shape. However, the cortical microtubule alignment along growth-derived maximal tensile stress in adjacent cells would mechanically isolate rapidly growing cells and limit their impact on organ shape. *In vivo*, we observed such microtubule response to stress and consistently found no significant effect of trichome number on sepal shape in wild-type and lines with trichome number defects. Conversely, modulating the microtubule response to stress in *katanin* and *spiral2* mutant made sepal shape dependent on trichome number, suggesting that, while mechanical signals are propagated around rapidly growing cells, the resistance to stress in adjacent cells mechanically isolates rapidly growing cells, thus contributing to organ shape reproducibility.

INTRODUCTION

Recent evidence suggests that stochasticity is widespread in cellular and molecular mechanisms [1]. In particular, growth is not uniform, and neighboring cells can grow at highly different rates, notably in plant tissues [2–5]. Differences in growth rates between organ domains are instrumental for the generation of shape diversity (e.g., [6, 7]). Heterogeneity in growth rates between adjacent cells may have the same role, albeit at a more local level. In fact, such local heterogeneities have been proposed to prime tissue invagination and mesoderm differentiation in *Drosophila* [8, 9] and to prime tissue folding and organogenesis in plants [5]. Conversely, how can such heterogeneity lead to reproducible organ size and shape?

In theory, morphogen gradients may provide a supracellular synchronizing cue within a given region, leading in the end to reproducible shapes [10–12]. Tissue structure and connectivity may also contribute to such synchronization, for instance, through cell rearrangements in animal tissues, or through differential plasmodesmata gating in plant tissues. However, even within tissue subdomains, adjacent cells can still display a high level of growth heterogeneity [2, 5]. Thus, reproducible shapes in the presence of growth heterogeneity could emerge from the combination of many, partially overlapping, supracellular gradients (e.g., [13]). While there is evidence that multiple morphogen gradients contribute to morphogenesis, such combinations might not be fine-grained enough to generate heterogeneity among individual cell. More pragmatically, because patterns of cell growth are not identical between individuals, growth heterogeneity cannot only be the result of a well-choreographed genetic regulation.

Mechanical signals have long been proposed to play a central role in the control of organ size and shape [14]. For instance, in organs where cells adhere to each other, differential growth generates mechanical conflicts between neighboring cells that impact final organ shape [15]. The accumulation of mechanical stresses was even proposed to trigger growth arrest at the level of a whole organ [16]. While this proposal is still debated, it may apply to the wing imaginal disc of *Drosophila*, where faster growth in the outer part of the disc compresses internal cells and would provoke an arrest in cell division [16, 17]. More recently, differential growth has been shown to trigger mechanical signals, leading to the activation of the Hippo signaling pathway in a positive feedback loop, and regulating growth [18]. In plants, such mechanical conflicts exist too. For instance, tensile stress between fast and slow growing regions was proposed to channel organ shape, through an impact of stress on microtubule and cellulose deposition [19]. While these studies show that mechanical stress can act as supracellular signal, they do not address the link between growth heterogeneity at the cell level and organ size and shape.

In theory, local mechanical conflicts between adjacent cells may add noise to morphogen-derived growth patterns [5]. In that scenario, such random processes would disturb stereotypic development and lead to abnormal individuals in the population. Because organ size and shapes are reproducible, while displaying heterogeneity at the cell level, this suggests instead that either noise is very low or that it is buffered. The exact contribution of the cell's response to such local mechanical conflicts in shaping organs remains unclear. On the one hand, it was proposed that a spatiotemporal averaging of cellular growth variability in sepal of *Arabidopsis* leads to precise organ shape. The averaging mechanism requires a reduced production of reactive oxygen species (ROS), and in the simplest scenario does not involve a mechanical feedback [20]. On the other hand, mechanical feedback from growth onto microtubule behavior has been proposed to amplify differences in growth rate between neighboring cells in the shoot apical meristem of *Arabidopsis* [5]. Based on these studies, mechanical feedback from growth heterogeneity may either not contribute to organ shape reproducibility, or could even increase growth heterogeneity with a questionable impact on organ shape reproducibility.

Here we investigate the relation between local mechanical conflicts and final shape using the *Arabidopsis* sepal (the outermost floral organ), as a model system, for its variability in cell type [21] and in cell growth rate [4, 19, 20] and for its remarkable final shape reproducibility.

RESULTS

Rapidly Growing Cells Induce a Circumferential Tensile Stress Pattern in Adjacent Cells

A local modification of the maximal stress directions in a tissue under tension, by ablating a cell, leads to a circumferential rearrangement of these principal stress directions around the ablation [22, 23]. At the level of the tissue each cell grows at its own rate and such growth heterogeneity may affect the local pattern of stress, notably because plant cells are glued to one another through their cell walls. To analyze the impact of rapidly growing cells on their neighbors, we chose trichomes (i.e., plant

hair cells) as an example. At the first stages of development, young trichomes exhibit localized rapid growth, leading to their bulging out of the epidermis surface [24].

Computational modeling allows us to explore several hypotheses and check the impact of a rapidly growing cell on the stress pattern in neighboring cells. We implemented a mechanical model of a tissue with 3D pressurized cells using the finite element method (FEM) (Figure 1), using the same simulation framework as [25] (Figures S1A–S1F). Cell walls are represented by triangular elastic membranes, which are deformed by the internal pressure within the cells. The walls of adjacent cell faces are connected by shared nodes, preventing cells from sliding past each other and transmitting mechanical forces from each cell to its neighbors. Mechanical stresses are computed at the level of each element forming the cell wall, based on the element resting shape, material properties and deformation (Figures S1A–S1F). At mechanical equilibrium, forces generated by the internal pressure and by the strain in cell walls balance each other. Growth is simulated by changing the resting shape of the elements based on their elastic deformation [26] and local values of a growth factor, following a Lockhart-type growth model [25, 27]: if the growth factor in a cell is null, elastic deformation of the cell walls will not result in any growth. When the growth factor is non-zero, the irreversible deformation (resultant growth) is proportional to the elastic deformation multiplied by the growth factor value.

There are several possibilities to explain the faster growth of an individual trichome cell. Turgor pressure could be higher in the trichome than its neighbors, causing the cell to swell (Figure 1). A difference in turgor pressure would require that there be no direct exchange of fluids between cells. Trichome cells are connected to their neighbors by plasmodesmata [28]. However, fluorescent tags have limited movement from young trichomes to surrounding cells. This suggests that the plasmodesmata could be gated [29], allowing pressure to build up at early stages of trichome development [30]. In our simulations of a growing tissue, a pressure of 2 MPa in the trichome compared to 0.5 MPa in the other cells was enough to cause the trichome to bulge into neighboring cells and result in a circumferential orientation of stress in those cells (Figures 1A and 1B). If we assume the tissue does not grow, a higher pressure difference is needed to obtain a similar stress pattern (Figure S1G).

Another possibility is that turgor pressure is equal within the tissue. In this case, tissue tension, combined with a locally softer cell wall could also explain the swelling of young trichome cells. We modeled the increased growth of a trichome by assigning it a cell wall that was three times softer, and simulating its growth by stress relaxation (Figure 1C). In the absence of tissue tension, this is not sufficient to obtain a clear re-orientation of the stresses around the cell (Figure 1D). In contrast, a prominent circumferential stress pattern can be observed around the growing trichome if we assume in addition that the whole tissue is stretched and under tension (Figures 1E and 1F). Qualitatively, this response remains the same when different cell shapes are assigned (Figures 1G–1I). Mechanical tension at the tissue level is known to occur in different plant organs [19–23, 31, 32] and could also play a role in the sepal epidermis [19]. From a tissue perspective, relaxing the walls in a single cell is comparable to ablating the cell, since it transfers part of the load to the neighboring cells.
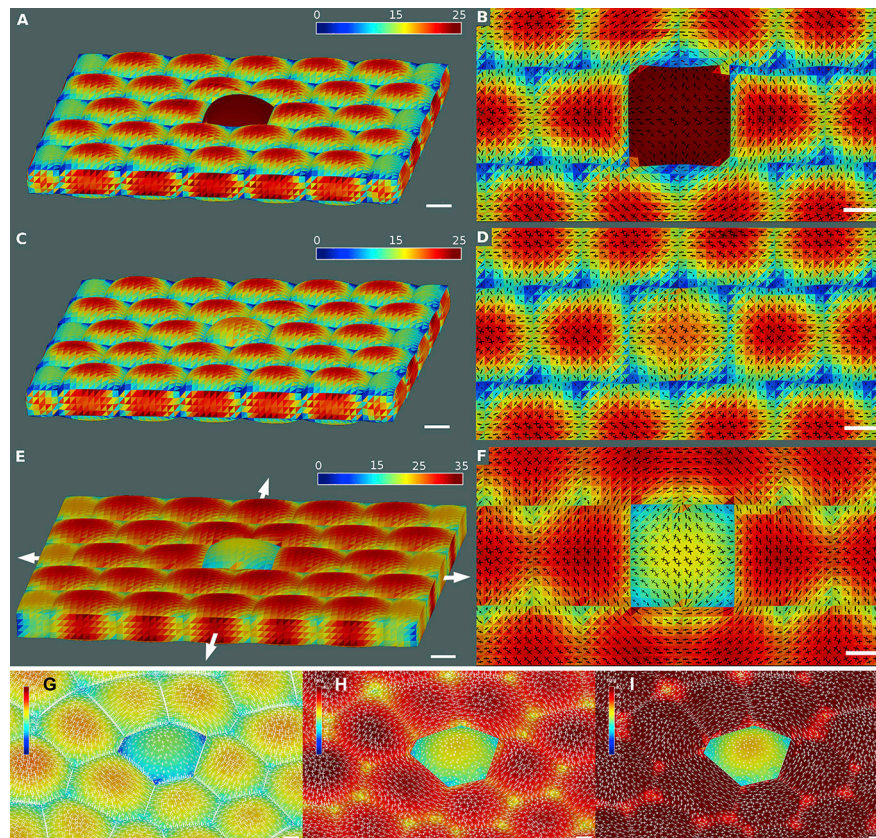
Figure 1. Mechanical Simulations of a Growing Tissue Layer

We used finite-element simulations to simulate the effects of a rapidly growing cell on its neighbors. Internal pressure within the cells causes an elastic (reversible) deformation of the walls. Some of the mechanical stress resulting from this deformation can be relaxed by allowing the elements to deform irreversibly, i.e., to grow.

(A) The central cell (i.e., the future trichome) is assigned a higher pressure (2 versus 0.5 MPa for other cells), resulting in larger elastic deformations and faster growth.

(B) A close up of the mechanical stresses around the trichome cell reveals a circumferential tensile stress pattern.

(C) Assuming a uniform pressure in the tissue, increased growth of the trichome cell can also be obtained with a softer cell wall (100 versus 300 MPa).

(D) The stresses around the cell show a less pronounced circumferential arrangement.

(E) Circumferential stress patterns become apparent once the whole tissue is stretched and allowed to grow.

(F) The fast-growing central cell relaxes stresses faster than its neighbors, resulting in stress concentration around it, similar to an ablated cell.

(G–I) Similar simulations as in (E) and (F) but with more realistic cell shapes, and for different wall stiffness values (trichome versus adjacent cells: G, 50 versus 150 MPa; H, 100 versus 300 MPa; I, 200 versus 600 MPa).

All simulations included 10 steps of stress relaxation. Crosses: principal directions of stress. Color bars, sum of local stresses in MPa. Arrows, stretch of tissue boundaries by 10% in each direction. Scale bars, 20 μm. See also Figure S1.

As with the cell softening case, cellular ablation will cause circumferential patterns of stresses only if the whole tissue is under tension ([23], Figures S1H–S1O). When combining higher turgor pressure in the central cell and the presence of tissue tension, the pattern of stress was reduced but a circumferential bias was still present (Figures S1L–S1O).

Therefore, although the effect is more or less pronounced depending on the cellular mechanism, rapidly growing cells will generate circumferential tensile stresses in adjacent cells.

Cortical Microtubules Reorient along Predicted Maximal Tensile Stress around Growing Trichomes

We tested the prediction that young trichome cells grow more rapidly and induce a circumferential stress pattern in adjacent cells experimentally. We use the abaxial sepal, which is the

farthest of the four sepals from the stem axis. Sepals exhibit substantial variability at the cell level [21], having a wide range of cell sizes and cell identities on the abaxial epidermis, while displaying roughly similar final shapes. Trichomes are one of the cell types present in the abaxial epidermis of the sepal (Figures 2A–2D). Importantly, trichomes emerge relatively late in sepal development. This means that, when trichomes emerge, average cell growth rates are lower in sepals than in leaves, where trichomes emerge very early in development. Although this implies that mechanical conflicts around trichomes might be less pronounced in sepals than in leaves, the late emergence of trichomes in sepals vastly facilitates the analysis of their emergence by confocal microscopy.

First, we confirmed that trichomes grow faster than their neighboring cells in sepals. To do so, we performed time-lapse
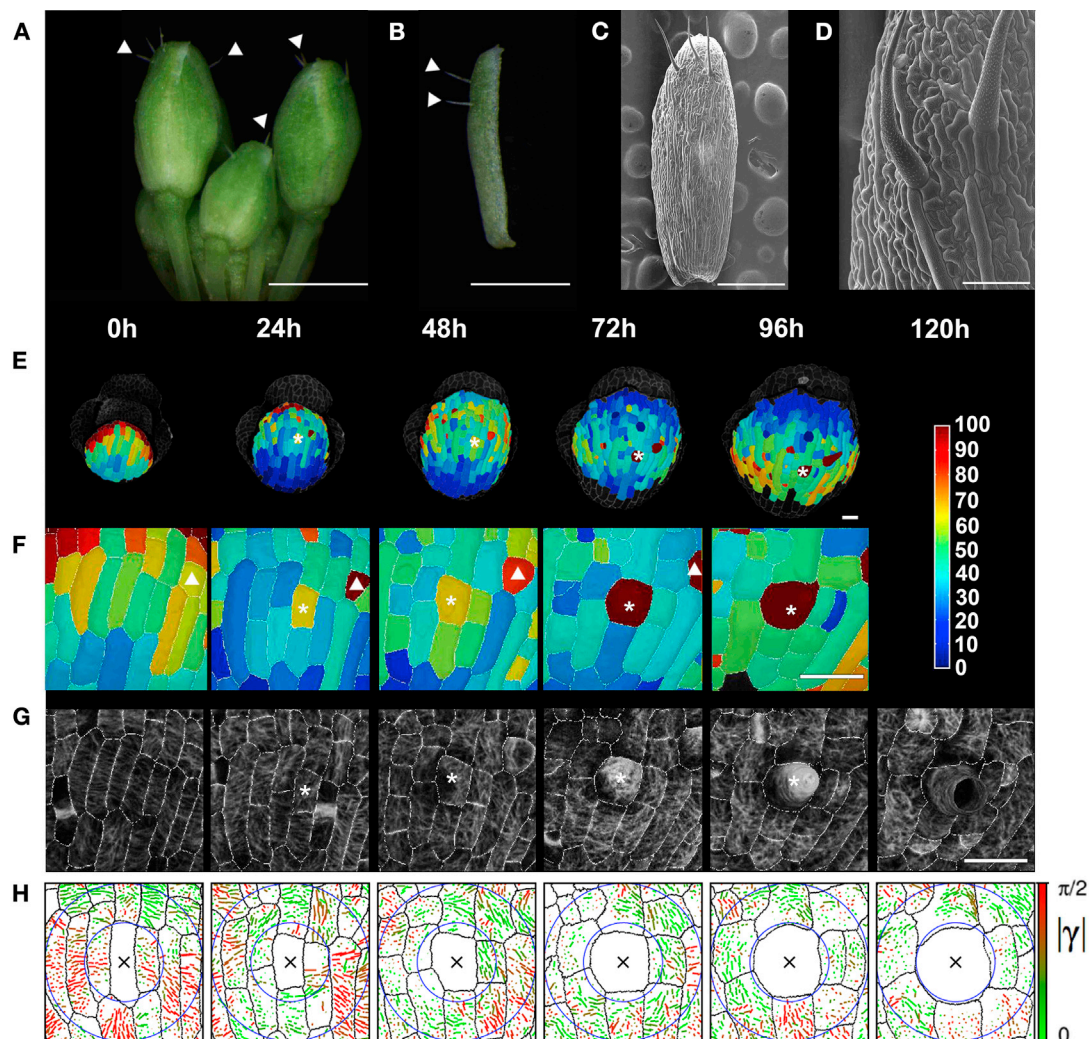
Figure 2. Circumferential Cortical Microtubule Orientation around a Rapidly Growing Trichome in Sepals

(A) Trichomes at the surface of floral buds (sepals) Scale bar, 0.5 mm.

(B) Trichomes on a dissected abaxial sepal. Scale bar, 0.5 mm

(C and D) SEM image of the surface of an abaxial sepal at low (C, scale bar, 300 μm) and high magnification (D, scale bar, 50 μm).

(E) Heatmap of area extension (%) over 24-hr intervals displayed on the first time point. Scale bar, 20 μm.

(F) Close up from (E): area extension (%) in region around a young trichome highlighted with a white star symbol. Scale bar, 20 μm. Note that the cell highlighted with a small white triangle is another trichome.

(G) Close up of the cortical microtubule organization at the surface of the abaxial sepal around a growing trichome. Scale bar, 20 μm.

(H) Results of anisotropy vectors of images shown in (G) γ represents the deviation of microtubules from a line tangent to a circle centered on the developing trichome. A geometric explanation of γ is given in Figure 3A. In short, the closer the angle γ is to zero (green color), the more the cortical microtubules are oriented circumferentially. Note a slight change of inclination between (G) and (H) in order to better visualize anisotropy vectors.

See also Figure S2.

imaging of emerging trichomes on the abaxial sepal expressing a fluorescent plasma membrane marker. We used MorphoGraphX [33] to segment cells in the epidermis for each time point and analyze their growth properties. As expected, we observed that trichome cells grow approximately twice as fast as their neighbors before they bulge out (Figures 2E and 2F). Although the number of time points once the trichome starts to elongate along the z axis (i.e., normal to sepal surface) is low, growth in the XY plane (i.e., tangential to sepal surface) seemed to decrease rapidly at that point.

We next investigated whether this local heterogeneity of growth rate leads to a mechanical conflict and a reorientation of principal stress directions as suggested in our model. Cortical microtubules align with predicted maximal tensile stress after artificial mechanical perturbations, like ablations or compressions, in the sepal [19] as well as in shoot meristems [22] and cotyledon pavement cells [23]. We thus used a microtubule marker (GFP-MBD) under the control of the CaMV35S promoter to visualize cortical microtubules as a readout of principal stress directions. The sub-cellular alignment of cortical microtubules

was then analyzed from curved 2D cell surfaces (also called 2.5D cell surfaces [33, 34]).

Qualitatively, we observed that cortical microtubules became circumferential around the trichome during the period of fast trichome growth and the cortical microtubule pattern then became more disorganized after the trichome bulged out (Figure 2G). To quantify this behavior, we used a subcellular nematic tensor-based tool to generate so-called cortical microtubule anisotropy segments that represent the orientations and strength of the cortical microtubule alignment in a local circle of radius 1 μm [34] (see STAR Methods).

As expected from our qualitative observation and as predicted in our model, we measured a significant bias toward circumferential orientations for cortical microtubules in the first ring around the growing trichome, i.e., between 10 and 20 μm around the center of the trichome before it bulged out (Figures 2H, 3A–3F, S2, and S3G, n = 5 sepals, 7 trichomes, 449 cells). Note that this response was less obvious in the outer ring, between 20 and 30 μm, around the center of the trichome (Figures 3G and S3H). Using this method, we also found that this circumferential organization became less obvious once the trichome bulged out (Figures 3F, S3G, and S3H).

The Cortical Microtubule Response to Growth-Induced Stress Can Be Modulated Genetically

To further test this response, we next used the *bot1-7*, katanin allele (in WS-4 ecotype), in which cortical microtubule response to mechanical perturbations is slower due to an impaired katanin-driven microtubule-severing activity [5, 19, 23]. As expected, cortical microtubule orientations around growing trichomes in *bot1-7* were not as clear cut as in the wild-type, at least qualitatively (Figure S3B). We next quantified the cortical microtubule behavior as shown above (see STAR Methods). Although cortical microtubules also became circumferential around a growing trichome in *bot1-7*, the response was slower and weaker during the growing phase of the trichome in the XY plane, when compared to the wild-type (Figures 3A, 3B, and S3, n = 5 sepals, 9 trichomes, 401 cells). Also consistent with slower cortical microtubule dynamics and a delayed response to stress, a bias toward a circumferential organization was still detected in *bot1-7*, but it appeared after the trichome bulged out (Figures 3F and S3). The statistical differences between WT and *bot1-7* were confirmed with a permutation test for the probability distribution of the weighted orientations O_i at each time point (see STAR Methods). The p values are summarized in Table S1.

Altogether these data (Figures 1, 2, and 3) suggest that the transient reorganization of cortical microtubules around a growing trichome is largely due to a modification of mechanical stress pattern and the ability of cortical microtubules to respond to this perturbation.

Because our model suggests that local growth heterogeneity may be buffered by the cell response to stress, we next analyzed the impact of the adjacent cell response to stress on local growth pattern. We measured $V_{area}^{\pm}$, the growth variability between trichome and neighbors, and N_{pos}, the number of neighbors growing more slowly than the trichome, before and after the trichome bulged out, and normalized to the total number of

neighbors N_{tot} (Figures 3H and 3I; see STAR Methods). In the wild-type, N_{pos} decreased rapidly before the trichome bulged out, suggesting that the directional reinforcement of the walls in the cells surrounding a trichome may constrain trichome growth in the XY plane (Figure 3H). To test that hypothesis, we performed the same analysis in the *bot1-7* mutant, which displayed a delayed microtubule response to stress. As expected, N_{pos} also decreased in *bot1-7*, but with a delay (Figure 3H). The statistical test is performed for $V_{area}^{\pm}$, and the p values are listed in Table S2.

The distributions of the averaged proportion of slower neighbors are statistically different between wild-type and *bot1-7*). Altogether, these results suggest that, while the microtubule response to growth-induced stress is transient in sepal trichomes, it is sufficient to have a local impact on growth.

Theory: Rapidly Growing Cells May Distort Organ Shape, Depending on the Ability of Adjacent Cells to Resist Local Stress

In an organ with an imposed growth pattern, the addition of noise, i.e., local growth heterogeneity, may in theory affect final organ shape. To test that hypothesis, we used a continuous, tissue-scale, finite element model of sepal growth, as in [20]. Note that such a two-dimensional model matches our focus on the epidermis and its growth-limiting role in shaping organs [31, 35].
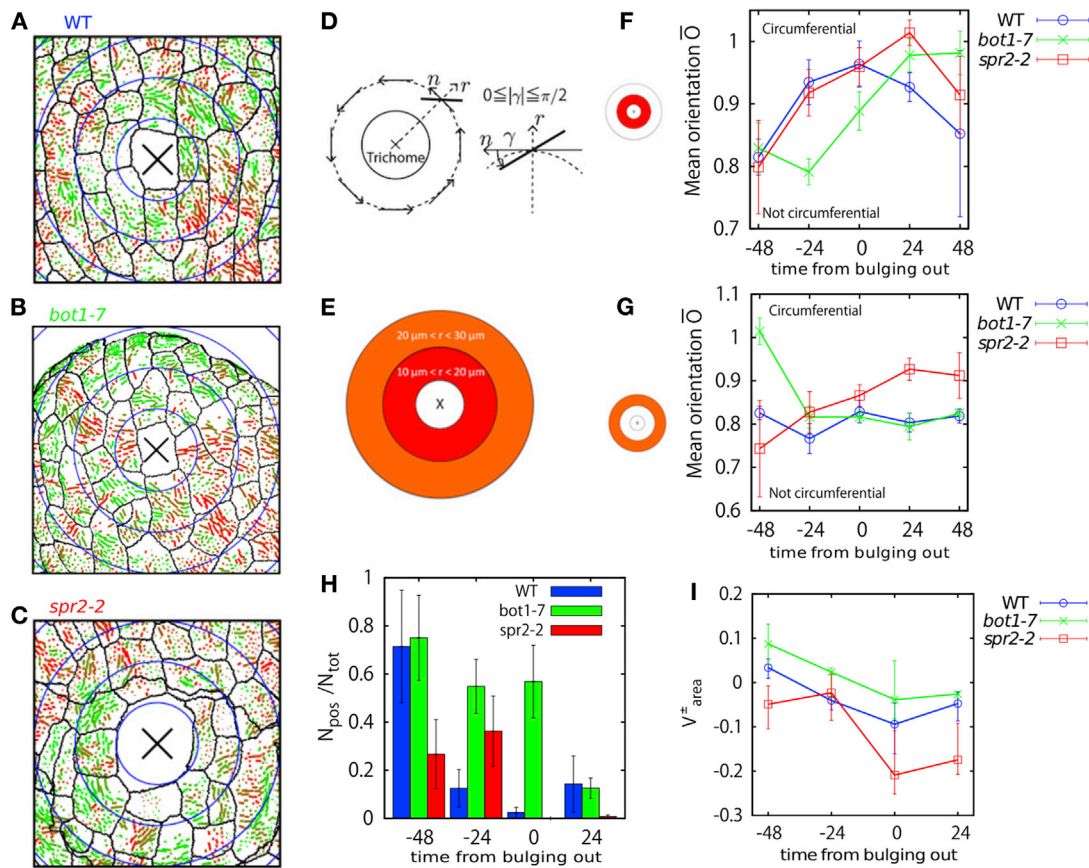
As expected, the addition of virtual trichomes (i.e., soft regions in an anisotropically stiffer field) at random position in the course of sepal growth led to modified final organ shapes. Sepal shapes became more variable when trichomes were added, and the width increased (Figure 4, no feedback [orange]). Note that the impact on width was proportionally higher than on length, consistent with the presence of an imposed anisotropic stiffness, matching the maximal proximo-distal growth bias observed in real sepals (Figure S4).

Next, we investigated whether mechanical resistance of cells adjacent to a rapidly growing cell would limit the impact on organ shape. To do so, when a trichome was added, we also included a stiff ring around it, mimicking the consequence of a local mechanical feedback from trichome growth onto cortical microtubules in neighboring cells (Figure 4, with feedback [purple]). In that case, the impact of trichomes on final organ shape was dramatically reduced.

Altogether, these results suggest that, while local growth heterogeneities may affect organ shape reproducibility, a mechanical reinforcement in cells neighboring rapidly growing cells can cancel that effect, thus contributing to organ shape reproducibility.

Sepal Width and Trichome Number Are Not Correlated, Except When the Cortical Microtubule Response to Stress Is Decreased in the Katanin Mutant

Because our organ-scale model predicts that the mechanical shielding of rapidly growing cells can counteract the impact of rapidly growing cells on organ shape reproducibility, we next analyzed sepal outlines with a previously described pipeline [20] and performed a morphometric analysis of the mature sepal shape to detect correlations with the number of trichomes in wild-type sepals. We focused our analysis on sepal width.

Figure 3. Quantification of the Local Impact of a Rapidly Growing Trichome on Adjacent Cells

(A–C) Close ups of quantified cortical microtubule alignment around rapidly growing trichome cells in wild-type (A), *bot1-7* (B), and *spr2-2* (C). Enlarged single panels have been reproduced from Figures 2 and S3 for ease of reading.

(D) Schematic explanation of the angle γ represented in Figure 2H.

(E) Schematic representation of distance chosen for the analysis. The black cross in the center represents the center of the trichome.

(F and G) Averaged cortical microtubule orientation in wild-type and *bot1-7*, before and after trichome starts to grow along the Z direction (bulging out) between 10 and 20 μm (F) and between 20 and 30 μm (G) from the center of the trichome. Time is in hours.

(H) Growth heterogeneity before and after trichome bulges out: N_{tot} is the number of total neighbors around trichomes at time t_i ; N_{pos} is the number of neighbors that grow slower than the trichome. The average of the ratio N_{pos}/N_{tot} over all trichomes provides a measure for how heterogeneous the growth is around trichome (i.e., the proportion of cases when the trichome grows faster than its neighbors, averaged over all trichomes).

(I) Dynamics of growth variability (see STAR Methods) in cell area in wild-type, *bot1-7*, and *spr2-2*.

See also Figure S3 and Tables S1 and S2.

Indeed, because sepals have less cells across their width than across their length when trichomes emerge, sepal width should be more impacted by the presence of trichomes, as predicted in our model. Furthermore, the gradient of growth along sepal length might dilute or even compensate the impact of trichomes on sepal length, making the interpretation of the results highly debatable (for the record, sepal length and aspect-ratio are displayed on Figure S5 and indeed show no consistent trend). In two wild-type ecotypes (*Col-0* and *WS-4*), we did not detect any significant correlation between the number of trichomes and sepal width (Figures 5 and S6, n = 186 *Col-0* sepals and n = 189 *WS-4* sepals).

To challenge that result, we also analyzed the relation between trichome number and sepal width in two lines (*35SR* and *gl3egl3*) with altered epidermal identity, and notably, in their ability to generate trichomes. In particular, we noticed that *Col-0* sepals

could never generate a high number of trichomes (in contrast to *WS-4* sepals) and when reaching the maximum number of trichomes, *Col-0* sepal shapes started to show a trend toward wider sepals (Figures 5 and S6). Strikingly, even in *35SR* line (in the Col-0 ecotype and with a high number of trichomes), we could not detect a significant impact of trichome number on sepal shape width (Figures 5 and S6, n = 118 *35SR* sepals, n = 165 *gl3egl3* sepals).

Because we cannot exclude the possibility that an even higher number of trichomes may affect sepal shape, we next investigated whether a reduced cortical microtubule response to stress in the katanin mutant would make sepal width dependent on trichome number. Although the effects were weak, we could detect a significant impact of trichome number on sepal width in the *katanin* mutant (Figures 5 and S6, n = 431 *bot1-7* sepals).
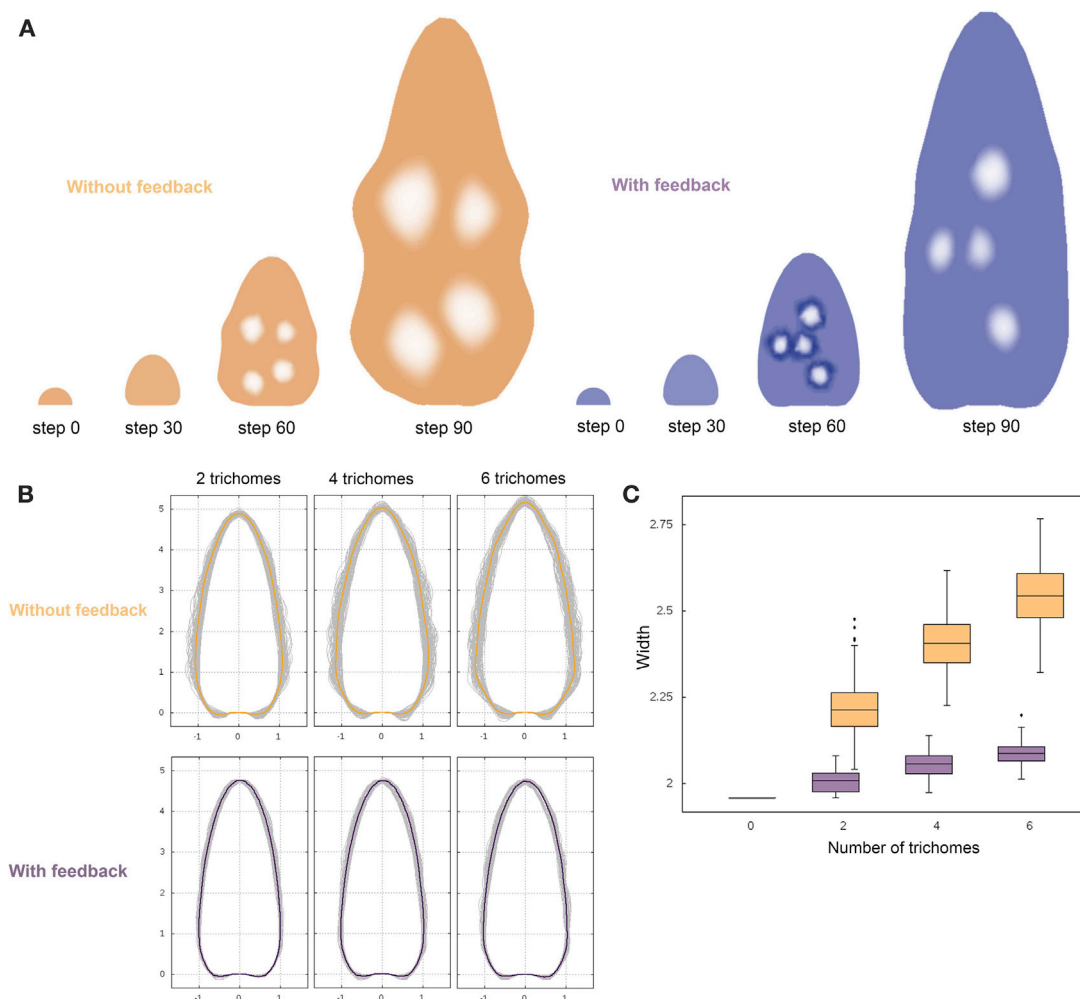
Figure 4. Predicted Impact of Trichomes on Final Sepal Shape, with or without Response to Tensile Stress

(A) Snapshots of numerical simulation without (left) and with (right) mechanical feedback. From time step 0 to step 50, the virtual sepal grows with a uniform and anisotropic stiffness. The stiffness in the sepal is transverse, i.e., orthogonal to the apico-basal growth axis. At time step 50, the trichomes are created at random positions in the sepal. The trichomes are modeled as disks of lower and isotropic stiffness. From the time steps 50–90, the inclusion of trichomes leads to modified shapes. At time step 70, the mechanical effect of trichomes is partly removed: in the whole sepal, the stiffness matrix is set to its value at the initial time step apart from the anisotropy of the trichomes that remains at zero. In the left panel (orange, no feedback), trichomes do not generate a mechanical reinforcement in neighboring regions, whereas, in the right panel (purple, with feedback), "feedback rings" (i.e., stiffer rings induced by the impact of trichome growth onto neighboring cells) surround trichomes from time steps 50–70. Each of these rings has an enhanced principal stiffness oriented circumferentially to the surrounded trichome.

(B) Normalized outlines showing variability in sepal shape for 100 simulations each. These are the results, from top to bottom and left to right, of numerical simulations without or with mechanical feedback and from 2 to 6 trichomes.

(C) Simulated sepal width for 2, 4, or 6 trichomes in absence (orange boxes) or presence (purple boxes) of feedback ring. For the boxplots, the box extends from the lower to the upper quartile values of the data, with a line at the median, and the whiskers extend past 1.5 of the interquartile range.

See also Figure S4 and Table S3.

Sepal Width and Trichome Number Are Correlated When the Cortical Microtubule Response to Stress Is Enhanced in *spiral2*

To further test this result, we conducted the same analysis in the *spiral2* mutant background. SPIRAL2/TORTIFOLIA is present at the sites of microtubule cross-overs and has been proposed to prevent microtubule severing at those sites [36–38]. The *spr2* mutation has recently been shown to promote the cortical microtubule response to mechanical perturbations both in shoot meristems and in sepals [19, 39]. We thus reasoned that, in a *spr2* mutant background, the cortical microtubule alignment around growing trichomes should be enhanced. In *spr2-2* (in Col-0 ecotype), we observed circumferential cortical microtubules around a growing trichome in the 10- to 20-μm ring as expected (Figures 3 and S3; Table S1; n = 10 sepals, 14 trichomes, 763 cells). However, when analyzing the more distant cells from the trichome center (20- to 30-μm ring), a bias toward circumferential cortical microtubules was present in *spr2-2*, whereas this could not be detected in the wild-type (Figures 3 and S3; Table S1).

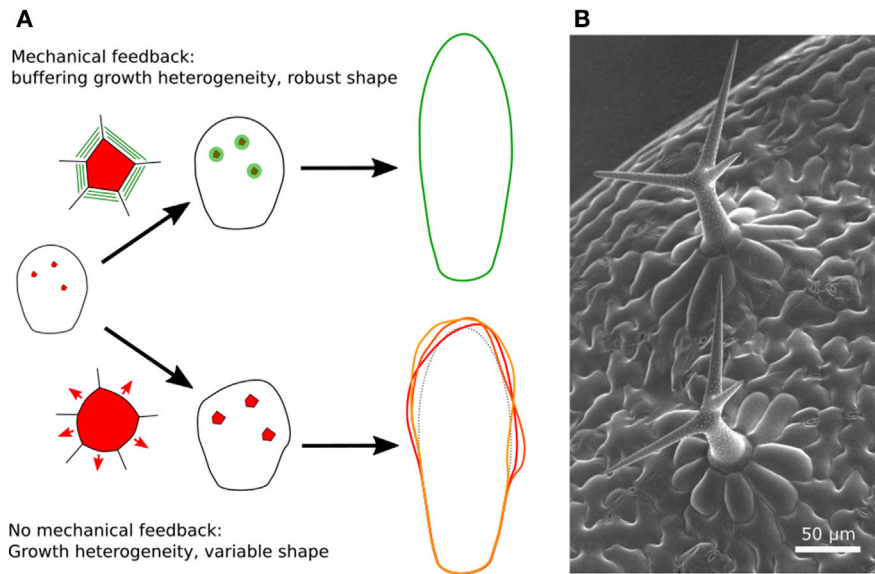**Figure 5. The Presence of Trichomes Does Not Affect Sepal Width in Wild-Type, *35SR*, and *gl3egl3* Lines but Impacts Sepal Width in *bot1-7* and *spr2-2***

(A) Superimposed outlines of mature stage 14 wild-type (WS-4, Col-0), *bot1-7* (in *WS-4*), *spr2-2* (in *Col-0*), *35SR* (in *Col-0*), and *gl3egl3* (in *Col-0*) sepals. Outlines were normalized by size to reveal differences in shape. The variation is the difference between the median outline (black) and that of the individual sepals (colored). Color scale bar represents the number of trichomes for each sepal outline; sepal contours are presented horizontally: sepal tip is always on the left side.

(B) Quantification of width in wild-type (WS-4, Col-0), *bot1-7* (in *WS-4*), *spr2-2* (in *Col-0*), *35SR* (in *Col-0*) and *gl3egl3* (in *Col-0*) sepals, in function of the number of trichomes per sepal (4 classes: no trichome, 1–3 trichomes, 4–8 trichomes, more than 8 trichomes). Error bars describe the 68% confidence interval of the median.

See also Figures S5 and S6.

The cortical microtubule circumferential alignment was also more stable in time in *spr2-2* than in the wild-type, as it was still observed even after the trichome cell bulged out, both in the 10- to 20-μm and 20- to 30-μm rings from the trichome center (Figures 3 and S3).

As for wild-type and *bot1-7*, we measured $V_{area}^{\pm}$, the growth variability between trichome and neighbors, and N_{pos}, the number of neighbors growing more slowly than the trichome, before and after the trichome bulged out, normalized to the total number of neighbors N_{tot} (Figures 3H and 3I, see STAR Methods). As in

Figure 6. Buffering Local Growth Heterogeneities through a Mechanical Feedback Leads to Reproducible Shapes
(A) Graphical summary of the main conclusion.
(B) Socket cells around trichomes in *Arabidopsis* leaves are elongated radially, i.e., perpendicular to the predicted microtubule and maximal tensile stress direction.

wild-type and *bot1-7*, N_{pos} in *spr2-2* decreased before the trichome bulged out, consistent with the cortical microtubule dependent constriction of trichome growth in the XY plane (Figure 3H; Table S2).

Interestingly, when analyzing sepal width in *spr2-2* mutant, we found it to be dependent on trichome number, only when trichome number was the highest (Figure 5, n = 186 *Col-0* sepals; n = 397 *spr2-2* sepals). Together with our results on katanin, this result further supports the idea that the cortical microtubule response to stress can modulate the impact of trichomes on sepal width. Because a larger population of adjacent cells is impacted around growing trichomes in *spr2-2*, the growth pattern would become more isotropic when trichome number increases, counteracting the global anisotropic growth of the sepal, thus increasing sepal width. Conversely, this suggests that the wild-type displays an optimal mechanical response to stress, strong enough to buffer local growth heterogeneity, but weak enough not to affect the global pattern of growth.

Coming back to our initial question, our results demonstrate that rapidly growing cells can impact the behavior of contiguous cells in sepals, notably through the microtubule response to mechanical signals. The consecutive mechanical shielding then buffers growth heterogeneity and thus contributes to organ shape reproducibility.

DISCUSSION

Our study on sepal trichomes suggests that differential growth between adjacent cells can generate a mechanical conflict with neighboring cells, which in turn locally and transiently impacts cortical microtubule orientations. Differential growth was already proposed to generate large-scale mechanical conflicts between different regions of a growing sepal [19]. A global

level of growth heterogeneity between adjacent cells had also been proposed to self-maintain through a mechanical feedback on microtubules in shoot apical meristems [5]. However, in both of these studies, the local response of cells to differential growth had not been investigated. The novelty of the present study resides in such local analysis: we demonstrate *in silico* and in experiments that two adjacent cells growing at different speeds can indeed respond to each other via a mechanical signal; the response of the neighboring cells constrains the rapidly growing cell and prevents it from distorting the tissue (Figure 6A). Interestingly in leaves, where trichomes are initiated much earlier than in sepals, socket cells surrounding trichomes are elongated radially (Figure 6B; e.g., [40]), consistent with the circumferential cortical microtubule orientation around young trichomes that we observed in sepals, and with a mechanical conflict arising in a context of faster growth rates.

Although we focus on the early phase of trichome development, the switch in growth vector from the XY plane to the Z direction may also represent a way to relieve stresses in the XY plane. In short, the socket cells would first resist rapidly growing trichome cells through mechanical shielding. This may transfer the load of stress from the socket cells to young trichome cells, which would then rearrange their cytoskeleton and growth pattern to accommodate this new mechanical status. The recent characterization of the coupling between cytoskeleton dynamics and cell wall properties in growing trichome [41] opens the path for such mechanical investigation.

Note that we only consider the mechanical implication of rapidly growing trichomes. Other factors such as hormones or small chemical species like ROS could be generated by the emerging trichome and lead to the reorganization of cortical microtubules. For instance, auxin [42] and ROS [43] were shown to affect cortical microtubule organization. In fact, because the

mechanotransduction pathway from growth-derived stress in trichome to cortical microtubule reorientation in neighboring cells is unknown, our data do not exclude the possibility that the initial mechanical conflict affects cortical microtubules through secondary signaling pathways.

Beyond the local impact of trichomes on cortical microtubules and growth in neighboring cells, we analyzed global sepal shapes in order to reveal the contribution of such local growth heterogeneities in organ shape reproducibility, and the associated stress-dependent buffering mechanism. Averaging variation in cellular growth over space and time is essential to achieve reproducible shape [20]. In fact, this is probably how growth heterogeneity is managed most often: if growth is spatially heterogeneous and if each cell oscillates between phases of fast and slow growth, growth becomes more homogeneous over long period on average, while retaining the ability to generate differential growth events. Our results on emerging trichomes address a case where temporal averaging does not occur: young trichome cells do not oscillate between slow and fast growth: young trichomes are growing rapidly for 36–48 hr, a relatively long period. How can the tissue manage such prolonged growth heterogeneity? Based on the absence of correlation between sepal width and trichome number in the wild-type, and the presence of a positive correlation between sepal width and trichome number in mutants with defective microtubule dynamics, we propose that the response of cortical microtubules around a rapidly growing cell restrains the propagation of mechanical stress, thus contributing to organ shape reproducibility. At this stage, we cannot completely rule out other scenarios, notably to explain why the katanin and *spiral2* mutants exhibit more variable sepal shapes. For instance, increased variability in sepal shape in these mutants may emerge from general defects in cell-cell coordination or compensation. However, in that scenario, the contribution of trichomes to organ shape variability would most likely be diluted. Because we detect a correlation between sepal width scales to trichome number when microtubule dynamics is impaired, we believe that our scenario remains the most parsimonious.

In our hands, we either detect no impact of trichome number on wild-type sepal shape, or a small impact of trichome number on sepal shape when cortical microtubule dynamics is affected. This suggests, as expected, that other mechanisms play a primary role in generating robust organ shapes. Beyond the existence of large-scale biochemical gradients (hormones, peptides, mRNA), large-scale mechanical conflicts are likely to help coordinate growth at a supracellular scale [44]. Indeed, there is accumulating evidence that large-scale mechanical signals contribute to shape reproducibility in plants and animals. For instance, in the *feronia* mutant, which is partly impaired in mechanoperception, the root growth pattern exhibits increased variability [45]. Similarly, the variability of neuron growth trajectory depends on the stiffness of their mechanical environment (e.g., [46]). The biased alignment of cortical microtubules at the sepal tip is following maximal tension at the sepal tip and emerges from a mechanical conflict between slow growing tip and fast-growing center of the sepal [19]. Our analysis of cortical microtubule and growth pattern around trichomes in the same organ allows us to propose that mechanical feedback on cortical microtubules has a dual role for organ shape reproducibility:

locally, mechanical signals are filtering out rapidly growing cells through local mechanical reinforcement, while globally mechanical signals provide a large-scale cortical microtubule alignment cue, in parallel to biochemical signals.

How general is this finding? While it is too early to tell, most tissues contain cells that maintain a specific growth rate for a prolonged time. Young trichomes do this most likely through wall softening and plasmodesmata gating [30]. Guard cells may constitute another example of such local and prolonged differential growth, since they stop growing earlier than their neighbors. In animal tissues, because the cell cycle can be much faster than in plants, mitosis may be long enough to trigger a mechanical response in neighboring cells. If so, one may predict that actomyosin would be recruited in these adjacent cells to provide mechanical shielding, similar to the microtubule/cellulose-based one in plants, thereby contributing to tissue and organ shape reproducibility.

STAR★METHODS

Detailed methods are provided in the online version of this paper and include the following:

- KEY RESOURCES TABLE
- CONTACT FOR REAGENT AND RESOURCE SHARING
- METHOD DETAILS
  - Plant Material and Growth Conditions
  - Live Imaging of the Growing Abaxial Sepal
  - SEM observation
  - Image Analysis
  - Sepal area measurements
  - Alignment of sepal center and orientation
  - Computational Modeling of a growing trichome in the epidermis
  - Computational modeling of sepal shape
  - CMT orientation around trichomes
  - Quantification of growth heterogeneity
  - Statistical test of CMT orientations and growth heterogeneity

SUPPLEMENTAL INFORMATION

Supplemental Information includes six figures and three tables and can be found with this article online at https://doi.org/10.1016/j.cub.2017.10.033.

REFERENCES

1. Meyer, H.M., and Roeder, A.H.K. (2014). Stochasticity in plant cellular growth and patterning. Front. Plant Sci. 5, 420.

2. Elsner, J., Michalski, M., and Kwiatkowska, D. (2012). Spatiotemporal variation of leaf epidermal cell growth: a quantitative analysis of Arabidopsis thaliana wild-type and triple cyclinD3 mutant plants. Ann. Bot. 109, 897–910.

3. Kierzkowski, D., Nakayama, N., Routier-Kierzkowska, A.-L., Weber, A., Bayer, E., Schorderet, M., Reinhardt, D., Kuhlemeier, C., and Smith, R.S. (2012). Elastic domains regulate growth and organogenesis in the plant shoot apical meristem. Science 335, 1096–1099.

4. Tauriello, G., Meyer, H.M., Smith, R.S., Koumoutsakos, P., and Roeder, A.H.K. (2015). Variability and constancy in cellular growth of Arabidopsis sepals. Plant Physiol. 169, 2342–2358.

5. Uyttewaal, M., Burian, A., Alim, K., Landrein, B., Borowska-Wykręt, D., Dedieu, A., Peaucelle, A., Ludynia, M., Traas, J., Boudaoud, A., et al. (2012). Mechanical stress acts via katanin to amplify differences in growth rate between adjacent cells in Arabidopsis. Cell 149, 439–451.

6. Cui, M.-L., Copsey, L., Green, A.A., Bangham, J.A., and Coen, E. (2010). Quantitative control of organ shape by combinatorial gene activity. PLoS Biol. 8, e1000538.

7. Aigouy, B., Farhadifar, R., Staple, D.B., Sagner, A., Röper, J.-C., Jülicher, F., and Eaton, S. (2010). Cell flow reorients the axis of planar polarity in the wing epithelium of Drosophila. Cell 142, 773–786.

8. Martin, A.C., Kaschube, M., and Wieschaus, E.F. (2009). Pulsed contractions of an actin-myosin network drive apical constriction. Nature 457, 495–499.

9. Pouille, P.-A., Ahmadi, P., Brunet, A.-C., and Farge, E. (2009). Mechanical signals trigger Myosin II redistribution and mesoderm invagination in Drosophila embryos. Sci. Signal. 2, ra16.

10. Jaeger, J., Irons, D., and Monk, N. (2008). Regulative feedback in pattern formation: towards a general relativistic theory of positional information. Development 135, 3175–3183.

11. Kuchen, E.E., Fox, S., de Reuille, P.B., Kennaway, R., Bensmihen, S., Avondo, J., Calder, G.M., Southam, P., Robinson, S., Bangham, A., and Coen, E. (2012). Generation of leaf shape through early patterns of growth and tissue polarity. Science 335, 1092–1096.

12. Nelissen, H., Rymen, B., Jikumaru, Y., Demuynck, K., Van Lijsebettens, M., Kamiya, Y., Inzé, D., and Beemster, G.T.S. (2012). A local maximum in gibberellin levels regulates maize leaf growth by spatial control of cell division. Curr. Biol. 22, 1183–1187.

13. Zagorski, M., Tabata, Y., Brandenberg, N., Lutolf, M.P., Tkačik, G., Bollenbach, T., Briscoe, J., and Kicheva, A. (2017). Decoding of position in the developing neural tube from antiparallel morphogen gradients. Science 356, 1379–1383.

14. Thompson, D.W. (1917). On Growth and Form (Cambridge University press).

15. Coen, E., and Rebocho, A.B. (2016). Resolving conflicts: modeling genetic control of plant morphogenesis. Dev. Cell 38, 579–583.

16. Shraiman, B.I. (2005). Mechanical feedback as a possible regulator of tissue growth. Proc. Natl. Acad. Sci. USA 102, 3318–3323.

17. Aegerter-Wilmsen, T., Aegerter, C.M., Hafen, E., and Basler, K. (2007). Model for the regulation of size in the wing imaginal disc of Drosophila. Mech. Dev. 124, 318–326.

18. Pan, Y., Heemskerk, I., Ibar, C., Shraiman, B.I., and Irvine, K.D. (2016). Differential growth triggers mechanical feedback that elevates Hippo signaling. Proc. Natl. Acad. Sci. USA. Published online October 26, 2016. https://doi.org/10.1073/pnas.1615012113.

19. Hervieux, N., Dumond, M., Sapala, A., Routier-Kierzkowska, A.-L., Kierzkowski, D., Roeder, A.H.K., Smith, R.S., Boudaoud, A., and Hamant, O. (2016). A mechanical feedback restricts sepal growth and shape in Arabidopsis. Curr. Biol. 26, 1019–1028.

20. Hong, L., Dumond, M., Tsugawa, S., Sapala, A., Routier-Kierzkowska, A.-L., Zhou, Y., Chen, C., Kiss, A., Zhu, M., Hamant, O., et al. (2016). Variable cell growth yields reproducible organdevelopment through spatiotemporal averaging. Dev. Cell 38, 15–32.

21. Roeder, A.H.K., Chickarmane, V., Cunha, A., Obara, B., Manjunath, B.S., and Meyerowitz, E.M. (2010). Variability in the control of cell division underlies sepal epidermal patterning in Arabidopsis thaliana. PLoS Biol. 8, e1000367.

22. Hamant, O., Heisler, M.G., Jönsson, H., Krupinski, P., Uyttewaal, M., Bokov, P., Corson, F., Sahlin, P., Boudaoud, A., Meyerowitz, E.M., et al. (2008). Developmental patterning by mechanical signals in Arabidopsis. Science 322, 1650–1655.

23. Sampathkumar, A., Krupinski, P., Wightman, R., Milani, P., Berquand, A., Boudaoud, A., Hamant, O., Jönsson, H., and Meyerowitz, E.M. (2014). Subcellular and supracellular mechanical stress prescribes cytoskeleton behavior in Arabidopsis cotyledon pavement cells. eLife 3, e01967.

24. Hülskamp, M. (2004). Plant trichomes: a model for cell differentiation. Nat. Rev. Mol. Cell Biol. 5, 471–480.

25. Bassel, G.W., Stamm, P., Mosca, G., Barbier de Reuille, P., Gibbs, D.J., Winter, R., Janka, A., Holdsworth, M.J., and Smith, R.S. (2014). Mechanical constraints imposed by 3D cellular geometry and arrangement modulate growth patterns in the Arabidopsis embryo. Proc. Natl. Acad. Sci. USA 111, 8685–8690.

26. Goriely, A., Robertson-Tessi, M., Tabor, M., and Vandiver, R. (2008). Elastic growth models. In Mathematical Modelling of Biosystems, R.P. Mondaini, and P.M. Pardalos, eds. (Springer), pp. 1–44.

27. Lockhart, J.A. (1965). An analysis of irreversible plant cell elongation. J. Theor. Biol. 8, 264–275.

28. Faulkner, C., Akman, O.E., Bell, K., Jeffree, C., and Oparka, K. (2008). Peeking into pit fields: A multiple twinning model of secondary plasmodesmata formation in tobacco. Plant Cell 20, 1504–1518.

29. Christensen, N.M., Faulkner, C., and Oparka, K. (2009). Evidence for unidirectional flow through plasmodesmata. Plant Physiol. 150, 96–104.

30. Ruan, Y.L., Llewellyn, D.J., and Furbank, R.T. (2001). The control of single-celled cotton fiber elongation by developmentally reversible gating of plasmodesmata and coordinated expression of sucrose and K+ transporters and expansin. Plant Cell 13, 47–60.

31. Kutschera, U., and Niklas, K.J. (2007). The epidermal-growth-control theory of stem elongation: an old and a new perspective. J. Plant Physiol. 164, 1395–1409.

32. Hejnowicz, Z., Rusin, A., and Rusin, T. (2000). Tensile tissue stress affects the orientation of cortical microtubules in the epidermis of sunflower hypocotyl. J. Plant Growth Regul. 19, 31–44.

33. Barbier de Reuille, P., Routier-Kierzkowska, A.-L., Kierzkowski, D., Bassel, G.W., Schüpbach, T., Tauriello, G., Bajpai, N., Strauss, S., Weber, A., Kiss, A., et al. (2015). MorphoGraphX: a platform for quantifying morphogenesis in 4D. eLife 4, 05864.

34. Tsugawa, S., Hervieux, N., Hamant, O., Boudaoud, A., Smith, R.S., Li, C.-B., and Komatsuzaki, T. (2016). Extracting subcellular fibrillar alignment with error estimation: application to microtubules. Biophys. J. 110, 1836–1844.

35. Savaldi-Goldstein, S., Peto, C., and Chory, J. (2007). The epidermis both drives and restricts plant shoot growth. Nature 446, 199–202.

36. Buschmann, H., Fabri, C.O., Hauptmann, M., Hutzler, P., Laux, T., Lloyd, C.W., and Schäffner, A.R. (2004). Helical growth of the Arabidopsis mutant

tortifolia1 reveals a plant-specific microtubule-associated protein. Curr. Biol. *14*, 1515–1521.

37. Shoji, T., Narita, N.N., Hayashi, K., Asada, J., Hamada, T., Sonobe, S., Nakajima, K., Hashimoto, T., and Hashimoto, T. (2004). Plant-specific microtubule-associated protein SPIRAL2 is required for anisotropic growth in Arabidopsis. Plant Physiol. *136*, 3933–3944.

38. Wightman, R., Chomicki, G., Kumar, M., Carr, P., and Turner, S.R. (2013). SPIRAL2 determines plant microtubule organization by modulating microtubule severing. Curr. Biol. *23*, 1902–1907.

39. Louveaux, M., Rochette, S., Beauzamy, L., Boudaoud, A., and Hamant, O. (2016). The impact of mechanical compression on cortical microtubules in Arabidopsis: a quantitative pipeline. Plant J. *88*, 328–342.

40. Valdivia, E.R., Chevalier, D., Sampedro, J., Taylor, I., Niederhuth, C.E., and Walker, J.C. (2012). DVL genes play a role in the coordination of socket cell recruitment and differentiation. J. Exp. Bot. *63*, 1405–1412.

41. Yanagisawa, M., Desyatova, A.S., Belteton, S.A., Mallery, E.L., Turner, J.A., and Szymanski, D.B. (2015). Patterning mechanisms of cytoskeletal and cell wall systems during leaf trichome morphogenesis. Nat. Plants *1*, 15014.

42. Sassi, M., Ali, O., Boudon, F., Cloarec, G., Abad, U., Cellier, C., Chen, X., Gilles, B., Milani, P., Friml, J., et al. (2014). An auxin-mediated shift toward growth isotropy promotes organ formation at the shoot meristem in Arabidopsis. Curr. Biol. *24*, 2335–2342.

43. Livanos, P., Galatis, B., and Apostolakos, P. (2014). The interplay between ROS and tubulin cytoskeleton in plants. Plant Signal. Behav. *9*, e28069.

44. Kennaway, R., Coen, E., Green, A., and Bangham, A. (2011). Generation of diverse biological forms through combinatorial interactions between tissue polarity and growth. PLoS Comput. Biol. *7*, e1002071.

45. Shih, H.-W., Miller, N.D., Dai, C., Spalding, E.P., and Monshausen, G.B. (2014). The receptor-like kinase FERONIA is required for mechanical signal transduction in Arabidopsis seedlings. Curr. Biol. *24*, 1887–1892.

46. Sur, S., Newcomb, C.J., Webber, M.J., and Stupp, S.I. (2013). Tuning supramolecular mechanics to guide neuron development. Biomaterials *34*, 4749–4757.

47. Hecht, F. (2012). New development in FreeFem++. J. Numer. Math. *20*, 251–265.

48. Hamant, O., Das, P., and Burian, A. (2014). Time-lapse imaging of developing meristems using confocal laser scanning microscope. Methods Mol. Biol. *1080*, 111–119.

49. Goodall, C.R., and Green, P.B. (1986). Quantitative analysis of surface growth. Bot. Gaz. *147*, 1–15.

STAR★METHODS

KEY RESOURCES TABLE

REAGENT or RESOURCE	SOURCE	IDENTIFIER
Experimental Models: Organisms/Strains		
p35S::GFP-MBD	[19]	N/A
pUQ10::Lti6b- 2xmCherry	[19]	N/A
botero1-7	[5, 19]	N/A
spiral2-2	[5, 19]	N/A
Software and Algorithms		
MorphoGraphX	[33]	N/A
Fibriltool (ImageJ macro)	[34]	N/A
FreeFem++	[47]	N/A

CONTACT FOR REAGENT AND RESOURCE SHARING

Further information and requests for resources and reagents should be directed to and will be fulfilled by the Lead Contact, Olivier Hamant (olivier.hamant@ens-lyon.fr).

METHOD DETAILS

Plant Material and Growth Conditions

Plants were grown on soil in a phytotron under short-day conditions (8 hr/16 hr light/dark period) for 4 weeks and then transferred to long-day conditions (16 hr/8 hr light/dark period). The microtubule reporter line *p35S::GFP-MBD* (WS-4) and the membrane reporter line *pUQ10::Lti6b- 2xmCherry* (Col-0) were described previously [19]. The *botero1-7* (katanin loss of function mutant allele) and *spiral2-2* mutants were previously described [5] [19].

Live Imaging of the Growing Abaxial Sepal

1- to 2-cm-long main inflorescence stems were cut from the plant. To access young buds, the first 10–15 flowers were dissected out and the stem was then kept in an apex culture medium [48] supplemented with 6-benzylaminopurine (900 mg/L). Twenty-four hours after dissection, the young buds were imaged with an SP8 laser-scanning confocal microscope (Leica) using long-distance 25x (NA 0.95) water-dipping objectives.

SEM observation

Scanning Electron Microscopy images of sepals from stage 14 flowers (Figure 2) and leaves (Figure 6) were acquired using a Hirox mini SEM 3000. Uncoated living sepal and leaf samples were placed in the SEM chamber without any further treatment (environmental SEM).

Image Analysis

Images were processed with MorphoGraphX 3D image analysis software [33]. Cortical microtubules orientation was analyzed as described in [34].

Sepal area measurements

Sepals dissected from stage 14 flowers were flattened between two slides and photographed on a black background using a dissecting microscope mounted with a camera. Custom Python programs were used to extract each sepal's outline from the sepal photos and to measure sepal's area. Briefly, images were segmented using the watershed method. Outlines were extracted and aligned along their longest axis determined by a polar Fourier transformation of the outline points (see below for sepal orientation).

Alignment of sepal center and orientation

The alignment of the center and orientation of the sepal allows us to estimate the sepal width and length, and allows comparison of different sepals. Given the sepal's outline points, $(x_1, y_1), \ldots, (x_N, y_N)$, where N is the number of outline points, the center of the outline is chosen to be the center of mass of the outline points, $(x_c, y_c) = (1/N \sum_{i=1}^{N} x_i, 1/N \sum_{i=1}^{N} y_i)$. The radial distance $r(\theta)$ of the outline points from the center is then evaluated as a function of polar angle θ. In order to fix the rotational degree of freedom (orientation), we employ

the polar Fourier transformation of the radial distance as $r(\theta) = r_o + \sum_{n=1}^{n_{max}} c_n \cos(n(\theta + \phi_n))$. Here $r_0 = 1/2\pi \int_0^{2\pi} r(\theta)d\theta$ is the average radius of the outline, n_{max} is chosen to be large enough such that the Fourier series well describe the function $r(\theta)$, and ϕ_n is the angular phase of the n-th Fourier mode. As the second harmonic $r_{2nd} = r_0 + \cos(2(\theta + \phi_2))$ represents a shape close to an ellipse with perpendicular long and short axes, we fix the orientation of the outline by choosing the convention $\phi_2 = 0$, implying that $\theta = 0$ corresponds to the long axis of the ellipse-like shape.

For outlines from the wild-type with distinct long (tip-to-bottom) and short (side-to-side) axes (see Figure 4A), there is no ambiguity in fixing the orientation to align the sepal along the long axis, which always corresponds to the tip-to-bottom direction. However, outlines from bot1-7 are quite round and special care is needed to unambiguously align the sepals. We observe that two dents always appear at the bottom of dissected bot1-7 sepals (see Figure 5A) that allows us to correctly distinguish the tip-to-bottom direction from the side-to-side direction.

After fixing the sepal orientation, the width is given by the distance between the outline points at $\theta = \pi/2$ and $\theta = 3\pi/2$, i.e., width equals to $r(\theta = \pi/2) + r(\theta = 3\pi/2)$. Similarly, the length is given by the distance between the outline points at $\theta = 0$ and $\theta = \pi$, i.e., length equals to $r(\theta = 0) + r(\theta = \pi)$.

Computational Modeling of a growing trichome in the epidermis

The cellular model construction follows [25], with some modifications as described below. The tissue template was generated in MorphoGraphX [33]. It contained 33 cells of dimensions $50 \times 50 \times 20$ μm, arranged in 5 rows. Cells were staggered to obtain realistic 3 way junctions. The whole template was divided into 22080 isosceles right triangles with 5 μm long sides. Individual triangles were assigned a thickness either of 0.5 μm or 1 μm, as described in Figures S1A–S1F. By default, the linearly hyperelastic triangular membrane elements were assigned a Young's modulus = 300 MPa, Poisson's ratio = 0.3 and internal pressure = 0.5 MPa. Tissue boundaries were free unless otherwise specified. We first used static (i.e., non-growing) simulations to test the effects of different parameters on the stress patterns at mechanical equilibrium. The internal pressure of the central cell was increased from 0.5 to 4 MPa by steps of 0.5 MPa, while all other parameters remained as default (Figures 1 and S1G). We then tested the effect of softening the cell wall in the central cell by assigning it a Young's modulus = 100 MPa, with an internal pressure of 0.5 MPa (Figure 1C). For growth simulations, the default growth factor was set to 0.1. Once the equilibrium configuration was found after applying internal pressure, the principal strains were computed for each triangle. The rest lengths of each triangle were then updated by adding the projection of principal strains on the triangles sides, multiplied by the growth factor. A new mechanical equilibrium was found at the end of each growth iteration. We simulated growth in a stretched tissue (Figure 1E) by restraining degrees of freedoms for displacement at the boundaries (Figure S1F). Boundary nodes were then displaced in the directions of width and length to simulate a stretch of 20%. The central cell was assigned a Young's modulus = 100 MPa and growth factor = 0.2, while pressure was set to default. A total a 5 growth steps were performed.

Computational modeling of sepal shape

We built a continuous mechanical model characterizing the influence of trichomes on sepal morphogenesis and the restriction of growth due to mechanical feedback. For this, we adapted the model introduced in [19] [20]. The ingredients of the model are as follows. Sepals are represented as two-dimensional media, because they mostly grow tangentially. Morphogenesis occurs by successive increments in area: the rest shape at step n is inflated by turgor pressure, P, leading to a new equilibrium shape, which is then used as a rest shape for the next step, $n+1$. This succession of elastic growth and stress release corresponds to the viscous relaxation of the sepal. The model was implemented in FreeFem++ [47].

The stiffness tensor relates the stress tensor, σ, to the strain tensor, ε, through the generalized Hooke's law. It is anisotropic, and characterized by a principal and a secondary stiffness direction, which are perpendicular. The components of the stress tensor along these directions (σ_{11}, σ_{22}, $\sigma_{12} = \sigma_{21}$) are related to those of the strain tensor through

$$\begin{pmatrix} \sigma_{11} \\ \sigma_{22} \\ \sigma_{12} \end{pmatrix} = \frac{E}{1-\nu^2} \begin{pmatrix} \dfrac{1}{1-a} & \nu & 0 \\ \nu & 1-a & 0 \\ 0 & 0 & \gamma \end{pmatrix} \begin{pmatrix} \varepsilon_{11} \\ \varepsilon_{22} \\ \varepsilon_{12} \end{pmatrix}$$

where the mean Young's (elastic) modulus E is the geometric mean of the Young's moduli along the principal stiffness direction $E_1 = E / (1-a)$ and the secondary stiffness direction $E_2 = E(1-a)$. a is the stiffness asymmetry, a dimensionless number contained in the interval [0, 1[and equal to 0 in the isotropic case. υ is the Poisson ratio. γ is a dimensionless number, equal to 1-υ in the isotropic case. In practice, we took $\gamma = 1-\upsilon$ in our simulations. In [19] [20] the expression of the elasticity matrix derives from the Hooke's law in 3D written in terms of the 3D Poisson ratio. For convenience, we considered the 2D Poisson ratio and adopted another definition for the anisotropy.

Initially, at time step 0, the sepal is shaped as half a disk of radius 1.1, the stiffness in the sepal is uniform and its principal stiffness direction is parallel to the straight edge of the disk. It then deforms and grows to reach its final shape at time step 90. From the initialization until the end of the simulation, the elastic properties of the medium, which are the coefficients of the above elasticity matrix and the principal stiffness orientation are advected. On top of the advection, the sepal mechanical properties are modified at time step 50 and time step 70.

At time step 50, trichomes are randomly included in the sepal. They are distributed at a distance greater than l_b from the sepal border and each trichome is distant of at least l_t from another trichome. They are distributed so that each possible configuration is equiprobable. The trichomes are modeled as disks of radius r with an isotropic stiffness ($a = 0$, E divided by 4). In half of the simulations, each trichome is in addition surrounded by a 'feedback' ring of thickness d in which the mean Young's modulus E and the anisotropy a are adjusted to double the principal Young's modulus E_1 and let the secondary Young's modulus E_2 unchanged, while the principal stiffness orientation is circumferential to the trichome.

At time step 70, the mechanical effect of trichomes is partly removed: in all the sepal the stiffness matrix is set to its value at the initial time step apart from the anisotropy of the trichomes that remains zero. The model parameters are recapitulated in Table S3.

CMT orientation around trichomes

We quantified the orientation of CMT anisotropy segments relative to the trichome as follows. First, we defined the center of the trichome cell as the center of mass of the intersections of the neighboring cells. Second, as depicted in Figure 3D, we defined the r-axis passing through the center of trichome and the center of the CMT anisotropy segment (thick line segment), and the n-axis that passes through the center of the CMT anisotropy segment and is perpendicular to the r-axis. By definition, the polar coordinate system (r, n) is determined by a distance and an angle of the center of the CMT anisotropy segment from the center of trichome. The r-axis and n-axis are always radial and circumferential, respectively, relative to center of the trichome.

Next we calculated the angle γ_i between the CMT anisotropy segment i and the n-axis. The absolute value $|\gamma_i|$ represents the degree of circumferential alignment of CMT anisotropy segments around a trichome ranged from 0 (circumferential) to $\pi/2$ (radial) (Figure 3D). To investigate the spatial trend of CMT anisotropy segments, we defined three circles, surrounding the center of the trichome, and with radii of 10, 20 and 30 μm, respectively (Figure 3E). Then we calculated the mean orientation of all CMT anisotropy segments between two consecutive circles (Figures 3F and 3G). Note that we use a weighted mean to account for anisotropy of the microtubule arrays: highly anisotropic arrays contribute more to the orientation. The weighted mean orientation around trichome is defined as follows,

$$\overline{O} = \frac{\sum_{i=1}^{N_v} \left(\frac{\pi}{2} - |\gamma_i| \right) w_i}{\sum_{i=1}^{N_v} w_i},$$

where N_v is the number of CMT anisotropy segments and w_i is the weight of CMT anisotropy segment i corresponding to the length of the CMT anisotropy segment. Randomized orientations should give a mean of $\pi/4$ (~ 0.8) with $N_v \rightarrow \infty$, circumferential orientations should give a mean superior to 0.8, and radial orientations, a mean inferior to 0.8. Note that we mix all the CMT anisotropy segments around different trichomes of same genotype together (N_v are about 1000~3000 segments at each time). The weighted standard deviation is defined as,

$$\sigma = \sqrt{\frac{\sum_{i=1}^{N_v} w_i \delta_i^2}{\sum_{i=1}^{N_v} w_i}}, \quad \delta_i = \left(\frac{\pi}{2} - |\gamma_i| \right) - \overline{O}.$$

The numbers of trichomes are $N_t = 7$ for wild-type, $N_t = 9$ for *bot 1-7* and $N_t = 14$ for *spr2-2*. The smaller the value of mean orientation $\overline{O}$, the lesser the CMTs orient circumferentially. The CMT anisotropy segment i satisfies $10 \ \mu m \leq r_i \leq 20 \ \mu m$ in Figure 3F (or $20 \ \mu m \leq r_i \leq 30 \ \mu m$ in Figure 3G).

Quantification of growth heterogeneity

In order to calculate the growth heterogeneity, we exclude the curvature effect as the trichome bulges in the Z axis (normal to sepal surface) because the growth of trichome surface area can be twice as much as those of neighboring cells as mentioned in the main text. Therefore, we considered the principal direction of growth (PDG) [33] [49] that describes how much a cell deforms on the XY plane (tangential to sepal surface). The 2×2 deformation matrix summarizes the deformation of the coordinates of "landmark" points in the sepal from the initial to the next time frame. We chose the landmark points as the intersections between neighboring cells. The PDG provides a stretch cross of which the long arm shows the maximum relative extension g_1 and the length of the short arm indicates the minimum relative extension g_2. Then, we can calculate the approximated growth in cell area on the XY plane as follows. We defined $g_1^{Tri}(t_i)$ and $g_2^{Tri}(t_i)$ as the maximum and minimum extension on the XY plane of the trichome at time t_i, and $g_1^j(t_i)$ and $g_2^j(t_i)$ as the maximum and minimum extension on the XY plane of the neighboring cell j of the trichome at time t_i. Then, the growth rate in cell area (AG) on the XY plane is given as:

$$AG^{Tri}(t_i) = \frac{g_1^{Tri}(t_{i+1}) g_2^{Tri}(t_{i+1})}{g_1^{Tri}(t_i) g_2^{Tri}(t_i)}, AG^j(t_i) = \frac{g_1^j(t_{i+1}) g_2^j(t_{i+1})}{g_1^j(t_i) g_2^j(t_i)}.$$

From these growth rates, we calculate the growth differences between trichome and neighboring cells. Note that the growth difference should be a dimensionless quantity because we want to compare them between different genotypes. Therefore, the normalized growth difference (D_j) between a trichome and neighboring cell j at time t_i can be defined as:

$$D_j(t_i) = \frac{AG^{Tri}(t_i) - AG^j(t_i)}{AG^{Tri}(t_i) + AG^j(t_i)}$$

The growth variability in cell area ($V_{area}^{\pm}$) can be evaluated by the average value of D_j over all the neighboring cells:

$$V_{area}^{\pm}(t_i) = \frac{1}{N_{tot}} \sum_{j=1}^{N_{tot}} D_j(t_i) = \frac{1}{N_{tot}} \sum_{j=1}^{N_{tot}} \frac{AG^{Tri}(t_i) - AG^j(t_i)}{AG^{Tri}(t_i) + AG^j(t_i)}.$$

where N_{tot} is the total number of neighboring cells surrounding a trichome. Since the growth variability quantifies the degree of growth difference between trichome and neighbors, it can be positive if the neighbors grow slower and negative if the neighbors grow faster. If we define the number of slower growing neighbors as N_{pos} in which $D_j(t_i) > 0$, we can calculate the growth heterogeneity N_{pos}/N_{tot} that describes how many neighboring cells grow slower than the trichome.

Statistical test of CMT orientations and growth heterogeneity

We used a permutation test to compare datasets of CMT orientations and growth heterogeneity between WT and *bot1-7,* and between WT and *spr2-2*. The samples are $(|\gamma_i|, w_i)$ in CMT orientations and the ratio N_{pos}/N_{tot} in growth heterogeneity. The null hypothesis is that the means (the weighted mean orientation $\overline{O}$ or the averaged N_{pos}/N_{tot} in the main text) of the two datasets have no difference. In the CMT orientation case, for instance between WT and *bot1-7* for the 10-20 μm ring at time 0, the numbers of data $(|\gamma_i|, w_i)$ are $N_{WT} = 3266$ for WT and $N_{bot1-7} = 3827$ for *bot1-7*. The two observed means are $\overline{O}(WT) = 0.980$ and $\overline{O}(bot1\text{-}7) = 0.890$ and their difference is $\Delta_{obs} = |0.980 - 0.890| = 0.09$. In permutation test, we put these two datasets together, and from the mixed distribution, we created the *m*-times permutated distribution $P_{WT}^{(m)}$ where we randomly picked up the number of data N_{WT} of $(|\gamma_i|, w_i)$ without replacement. We also define $P_{bot1-7}^{(m)}$ as the rest of the data remaining in the mixed distribution. Then we calculated the permutated difference $\Delta_p^{(m)} = \left|(\text{mean of } P_{WT}^{(m)}) - (\text{mean of } P_{bot1-7}^{(m)})\right|$. After the permutation trials performed $m = 10^4$ times, the p value is approximated by the percentage l/m where l is the number of trials which satisfy $\Delta_p^{(m)} > \Delta_{obs}$. We used this nonparametric approach because it does not require any knowledge of the distribution of $(|\gamma_i|, w_i)$. The significance level of the test was chosen as 0.05.